

# A fast and efficient deep learning procedure for tracking droplet motion in dense microfluidic emulsions

Mihir Durve,<sup>1,2</sup> Fabio Bonaccorso,<sup>1,3,4</sup> Andrea Montessori,<sup>1</sup>

Marco Lauricella,<sup>1</sup> Adriano Tiribocchi,<sup>1,3</sup> and Sauro Succi<sup>1,3,5</sup>

<sup>1</sup>*Center for Life Nano Science@La Sapienza, Istituto Italiano di Tecnologia,  
Viale Regina Elena, 291, 00161 Roma, Italy*

<sup>2</sup>*Quantitative Life Sciences Unit, The Abdus Salam International  
Centre for Theoretical Physics (ICTP), Trieste 34151, Italy*

<sup>3</sup>*Istituto per le Applicazioni del Calcolo CNR, via dei Taurini 19, Rome, Italy*

<sup>4</sup>*Department of Physics and INFN, University of Rome Tor Vergata,  
Via della Ricerca Scientifica 1, 00133, Rome, Italy*

<sup>5</sup>*Institute for Applied Computational Science,  
John A. Paulson School of Engineering and Applied Sciences,  
Harvard University, Cambridge, USA*

(Dated: March 3, 2021)

## Abstract

We present a deep learning-based object detection and object tracking algorithm to study droplet motion in dense microfluidic emulsions. The deep learning procedure is shown to correctly predict the droplets' shape and track their motion at competitive rates as compared to standard clustering algorithms, even in the presence of significant deformations. The deep learning technique and tool developed in this work could be used for the general study of the dynamics of biological agents in fluid systems, such as moving cells and self-propelled micro organisms in complex biological flows.

Keywords: Deep learning, YOLO and DeepSORT, Object recognition and tracking, Lattice Boltzmann approach, Dense emulsions.

## I. INTRODUCTION

In recent times, Machine Learning (ML) has gained enormous attention within the scientific community [1], as it provides a general automated framework to accomplish highly complex computational tasks through a self-improving trial and error minimization procedure [2].

Although often overhauled (for a critical assessment see [3, 4]), ML proves indeed successful in a number of tasks, such as object classification and image recognition [5, 6], handwriting recognition [7], text analysis [8, 9], voice recognition [10], and more recently also physical [11] and biological applications such as protein folding [12].

Machine learning algorithms perform these tasks by realising a model that outputs decisions or predictions starting from (big) data inputs which are used to train the network by recursive optimisation of its parameters (the weights connecting nodes of the network across two subsequent layers). A particularly successful instance of ML, called deep learning (DL), uses multi-layer artificial neural networks, as opposed to the so-called shallow networks, which consist of just a few hidden layers [13]. Deep learning-based approaches have been successfully employed in a number of applications, from medical diagnosis [14–17] to physics[11, 18]. In microfluidics, deep learning has been used to study physical systems and quality control processes. Mahdi et al. [19] used neural networks to predict the size of the droplets in an emulsion. Khor et al [20] developed a convolutional autoencoder model to discover a low-dimensional representation to describe droplet shapes within a concentrated emulsion and study the stability of droplets in an emulsion. Hadikhani et al [21] trained neural networks to estimate fluid and flow parameters by analysing digital images of fluid in microchips.

In recent years, high internal phase emulsions (HIPE) and soft flowing crystals, namely ordered states of flowing matter characterised by a highly ordered collection of liquid droplets arranged in crystal-like structures, are showing their potential in many fields of science and engineering. Indeed, due to the typical porous polymeric matrix (see figure 1 for two examples of emulsions in microfluidic channels (a) during the early stage formation and (b) at high packing fractions ), they can be efficiently employed in a wide range of advanced applications, such as catalyst supports, ion-exchange modules, separation media, electrochemical sensing, to name but a few. Moreover, they are very fit for bio-inspired applications such as

scaffolds in tissue engineering, where the interconnected pore structure is essential for their function. Besides their relevance for a host of applications in the fields mentioned above, soft porous materials also raise a fundamental challenge to non-equilibrium thermodynamics, since they display properties which cannot be traced back to any of the three basic states of matter. For instance, HIPEs are binary mixtures of immiscible liquids, each featuring linear Newtonian rheology, that exhibit highly non-Newtonian mechanical and rheological properties. Thus, a full-understanding of the rich dynamics underlying these classical many-body systems is required to optimise the microfluidic devices employed for their production and to fine-tune their properties for different purposes.

The aim of this work is to demonstrate that general deep learning-based tools can be adapted, tuned and profitably used to extract trajectories of droplets starting from digital frames of the fluid system, as obtained either by experiment or via computer simulations. The deep learning procedure is here applied to the case of dense flowing emulsions in microchannels to compute the paths followed by the droplets, as obtained via Lattice Boltzmann simulations. This represents a very first step towards a more complex task, consisting in the characterization of the dynamics of this many-body soft system in terms of effective equations of motion of the droplets flowing in the continuum phase.

The results are encouraging, in that the procedure proves capable of fast (about 400 frames/second) recognition and tracking of droplets with significant departures from the spherical shape. Given its flexibility, it is expected that the procedure developed in this paper can be readily generalized to the study of the dynamics of moving agents in micro and nanoflows of biological interest [22].

The paper is structured as follows. In the next section we describe the Machine Learning procedure and, shortly, the lattice Boltzmann method used to produce the validation data. Section III is dedicated to a discussion of the numerical results and some conclusive remarks close the paper.

## II. METHODS

In the following we provide details of the Machine Learning procedure as well as of the Lattice Boltzmann method, which is the simulation technique employed to produce the validation data. We begin by discussing the latter.

### A. Lattice Boltzmann method for dense emulsions

In this section we briefly describe the numerical model, namely an extended color-gradient approach with repulsive near-contact interactions, previously employed in Ref. [23–27]. In the multicomponent LB model, two sets of discrete distribution functions evolve via the usual streaming-collision algorithm (see [28, 29]):

$$f_i^k(\vec{x} + \vec{c}_i \Delta t, t + \Delta t) = f_i^k(\vec{x}, t) + \Omega_i^k[f_i^k(\vec{x}, t)] + S_i(\vec{x}, t), \quad (1)$$

In the above equation,  $f_i^k$  is the discrete distribution function, representing the probability of finding a particle of the  $k$ -th component at position  $\vec{x}$ , time  $t$  with discrete velocity  $\vec{c}_i$ , and  $S_i$  is a source term coding for the effect of external forces (such as gravity, near-contact interactions, etc).

In equation 1 the time step is taken as  $\Delta t = 1$ , and the index  $i$  runs over the discrete lattice directions  $i = 1, \dots, b$ , being  $b = 9$  for a two dimensional nine speed lattice (D2Q9). The density  $\rho^k$  of the  $k$ -th component and the total linear momentum of the mixture  $\rho \vec{u} = \sum_k \rho^k \vec{u}^k$  are obtained, respectively, via the zeroth and the first order moment of the lattice distributions  $\rho^k(\vec{x}, t) = \sum_i f_i^k(\vec{x}, t)$  and  $\rho \vec{u} = \sum_i \sum_k f_i^k(\vec{x}, t) \vec{c}_i$ . The collision operator splits into three parts [30, 31]:

$$\Omega_i^k = (\Omega_i^k)^{(3)} \left[ (\Omega_i^k)^{(1)} + (\Omega_i^k)^{(2)} \right]. \quad (2)$$

where  $(\Omega_i^k)^{(1)}$ , stands for the standard collisional relaxation [28],  $(\Omega_i^k)^{(2)}$  codes for the perturbation step [30], contributing to the buildup of the interfacial tension while  $(\Omega_i^k)^{(3)}$  is the recoloring step [30, 32], which promotes the segregation between the two species, minimising their mutual diffusion.

By performing a Chapman-Enskog multiscale expansion it can be shown that the hydrodynamic limit of Eq.1 is a set of equations for the conservation of mass and linear momentum (i.e., the Navier-Stokes equations), with a capillary stress tensor of the form:

$$\Sigma = -\tau \sum_i \sum_k (\Omega_i^k)^{(2)} \vec{c}_i \vec{c}_i = \frac{\sigma}{2|\nabla \rho|} (|\nabla \rho|^2 \mathbf{I} - \nabla \rho \otimes \nabla \rho) \quad (3)$$

being  $\tau$  the collision relaxation time, controlling the kinematic viscosity via the relation  $\nu = c_s^2(\tau - 1/2)$  ( $c_s = 1/\sqrt{3}$  the sound speed of the model) and  $\sigma$  is the surface tension [28, 29].

In eq. 3, the symbol  $\otimes$  denotes a dyadic tensor product. The stress-jump condition across a fluid interface is then augmented with an intra-component repulsive term aimed at condensing the effect of all the repulsive near-contact forces (i.e., Van der Waals, electrostatic, steric and hydration repulsion) acting on much smaller scales ( $\sim O(1 \text{ nm})$ ) than those resolved on the lattice (typically well above hundreds of nanometers). It takes the following form:

$$\mathbf{T}^1 \cdot \vec{n} - \mathbf{T}^2 \cdot \vec{n} = -\nabla(\sigma \mathbf{I} - \sigma(\vec{n} \otimes \vec{n})) - \pi \vec{n} \quad (4)$$

where  $\pi[h(\vec{x})]$  is responsible for the repulsion between neighbouring fluid interfaces,  $h(\vec{x})$  being the distance between interacting interfaces along the normal  $\vec{n}$ .

The additional term can be readily included within the LB framework, by adding a forcing term acting only on the fluid interfaces in near-contact, namely:

$$\vec{F}_{rep} = -A_h[h(\vec{x})]\vec{n}\delta_I \quad (5)$$

In the above,  $A_h[h(\vec{x})]$  is the parameter controlling the strength (force per unit volume) of the near-contact interactions,  $h(\vec{x})$  is the distance between the interfaces,  $\vec{n}$  is a unit vector normal to the interface and  $\delta_I \propto \nabla\phi$  is a function, proportional to the phase field  $\phi = \frac{\rho^1 - \rho^2}{\rho^1 + \rho^2}$ , employed to localize the force at the interface.

To conclude, the addition of the repulsive force (added to the right hand side of Eq. 1) naturally leads to the following (extended) conservation law for the momentum equation:

$$\frac{\partial \rho \vec{u}}{\partial t} + \nabla \cdot \rho \vec{u} \vec{u} = -\nabla p + \nabla \cdot [\rho \nu (\nabla \vec{u} + \nabla \vec{u}^T)] + \nabla \cdot (\boldsymbol{\Sigma} + \pi \mathbf{I}) \quad (6)$$

namely the Navier-Stokes equation for a multicomponent system, augmented with a surface-localized repulsive term, expressed through the gradient of the potential function  $\pi$ .

## B. Deep learning procedure

The Deep learning approach employed in this work consists of three basic steps: 1) Data preparation, 2) Network training and set-up, and 3) Inference (see Fig. 2), which we now discuss in some detail.

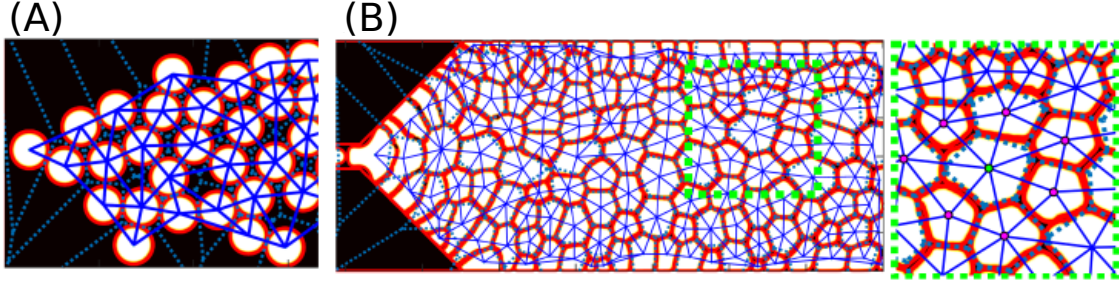


FIG. 1. LB simulation of (A) Early stage formation of soft flowing crystals in microchannel. (B) Flowing high internal phase emulsion in microfluidic channel with divergent inlet. Blue solid lines connecting centers of droplets result from a Delaunay triangulation, while dotted polygons are the associated Voronoi tessellation.

In order to extract trajectories of droplets from the digital images, the deep learning-based application must accomplish two tasks: i) identify the droplets and find their location in a given image, and ii) track the droplet displacements between successive frames. In our implementation, these two tasks are performed via two different algorithms: droplet detection makes use of YOLO [33, 34], a state-of-the-art, deep neural network algorithm for real-time object detection. The YOLO algorithm has been shown to be significantly faster than most other techniques for object detection and classification [34, 35]. The YOLO algorithm is highly accurate in detecting objects on interest in the images consisting of many objects and complex background scenarios. YOLO algorithm can be implemented on the CPU as well as GPUs to gain higher rate of image analysis (inference speed) making it a good choice for real-time video analysis. YOLO takes an image as an input and outputs a list of detected objects with their classes, confidence of detection, and their locations. This information is then passed to DeepSORT [36], an effective multi-object tracker, whose task is precisely to keep track of the detected objects as they move in time.

### 1. Data preparation

In order to identify droplets in a given image, the YOLO network must be trained with several examples, called training data set, which should have a wide enough statistical significance. Its preparation is arguably the most labour intensive task of the training phase and will have high impact on the validity of the whole procedure. For supervised learning

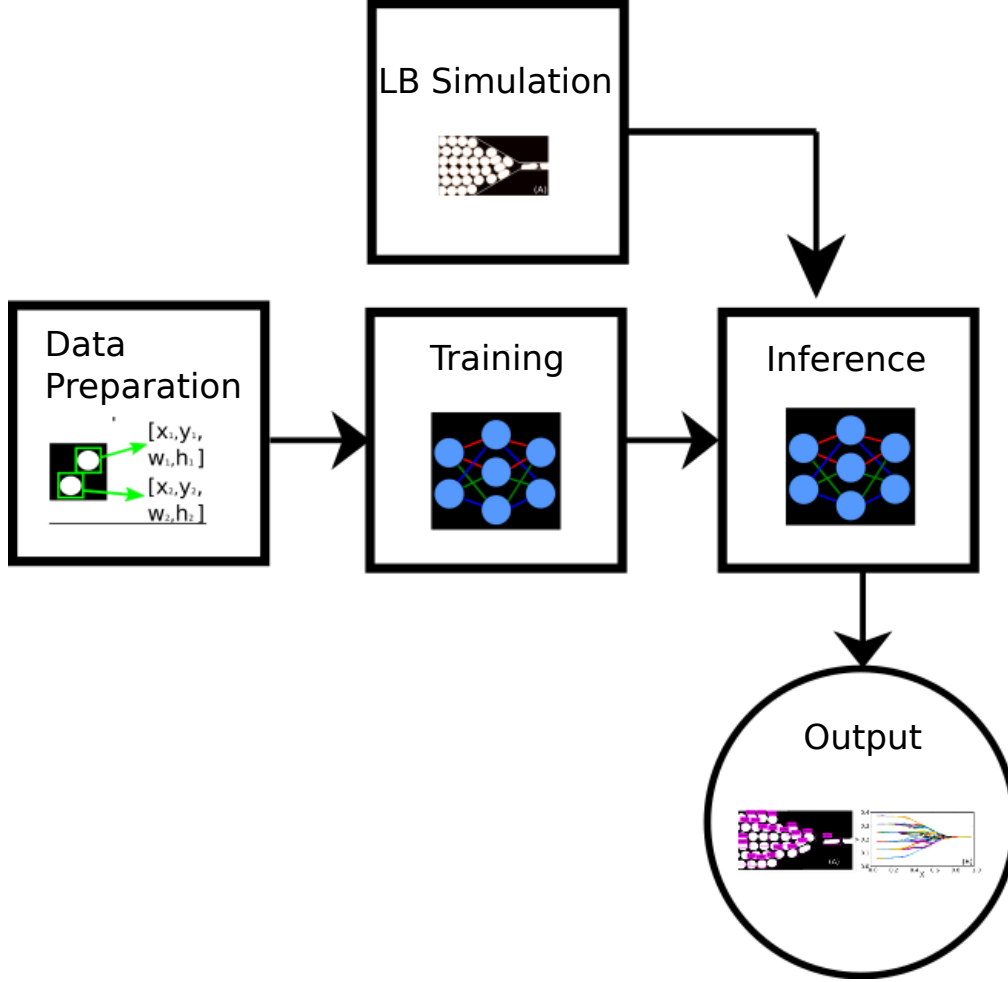


FIG. 2. The three basic steps involved in the deep learning based application for trajectory extraction of droplets in dense emulsions. From left to right: 1) Synthetic data preparation for the network training, 2) Network Training, 3) Inference and Validation based on the data provided by the LB simulation (top). The output is a set of droplets along with their trajectories (bottom).

algorithms, training data typically consist of inputs, such as images, and expected output of the network called *labels*. In order to train a network to identify droplets in an image, the training data must include several examples, each consisting of an image of a system with droplets, along with a text file containing their sizes (height and width) and centers positions ( $x$  and  $y$  coordinates) within the image as labels.

To generate the training data set, we prepared several images by randomly placing a fixed number (7) of droplets with varying aspect ratios in a uniformly dark background of size 1040 X 450 pixels, since this is the typical output of the LB simulations. For each sample,

we build the image and note the positions and sizes of all the droplets that we placed. An example from the training data set is shown in Fig. 3, along with the text file containing the labels of each droplet, namely the coordinate of its center and the height and width of its bounding box. The code to generate the training data is given in the data access sheet.

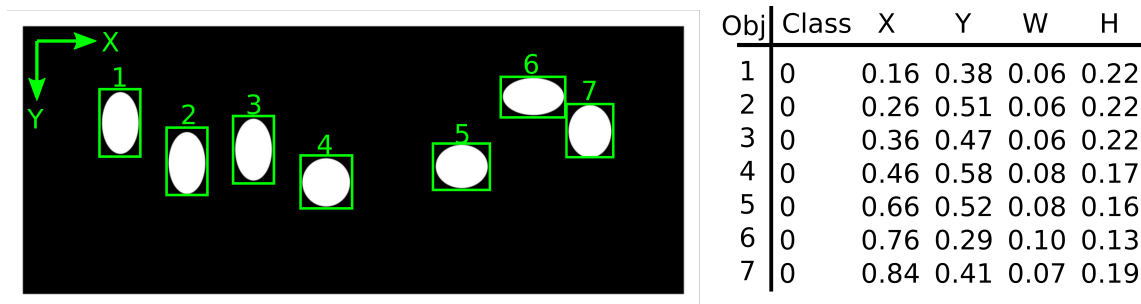


FIG. 3. A sample image from training data set with its label in the format needed to train YOLO network, namely the sequential number of the object, the class of the object (droplet), the coordinates of its center (x and y), the width (w) and height (h) of the bounding box.

## 2. Network training and set-up

The network set-up is performed by using Darknet [37], an open-source neural network framework written in C and CUDA and developed to support YOLO on both CPU and GPU devices: it supports the most common neural network operations such as convolution, max pooling, and various activation functions. Once the network is trained, the same framework can then be used as an inference engine.

For our task, we selected a predefined, ready to implement network architecture, known as yolov3-tiny, consisting of  $24$  layers, branching out in many convolutional and pooling layers with a total of approximately  $8$  million trainable parameters (weights). The training of the YOLO network was carried out by employing 10,000 training images as described above. For the training, we used GPU implementation of Darknet on a system consisting of NVIDIA RTX 2060 Super GPU, common in middle-level desktop configurations for gaming. The Github repository outlines the details to carry out training of the network [38] as well as in the data access sheet. The training operation is realized in many batches. In each batch, a fixed number of images (called batch size) are given as input to the network. Based on the predicted output of the network, a loss function is calculated, and the parameters of



the network are then updated to minimize it. The YOLO algorithm uses a multi-component loss function [33, 34] accounting for the errors in classifying detected objects, locating the objects, as well as error in prediction confidence for the detected objects. The chosen values of parameters for the training (batches, batch size, etc.) can be found in [39]. As the training progresses, the total loss decreases to a near-zero value, as shown in Fig. 4.

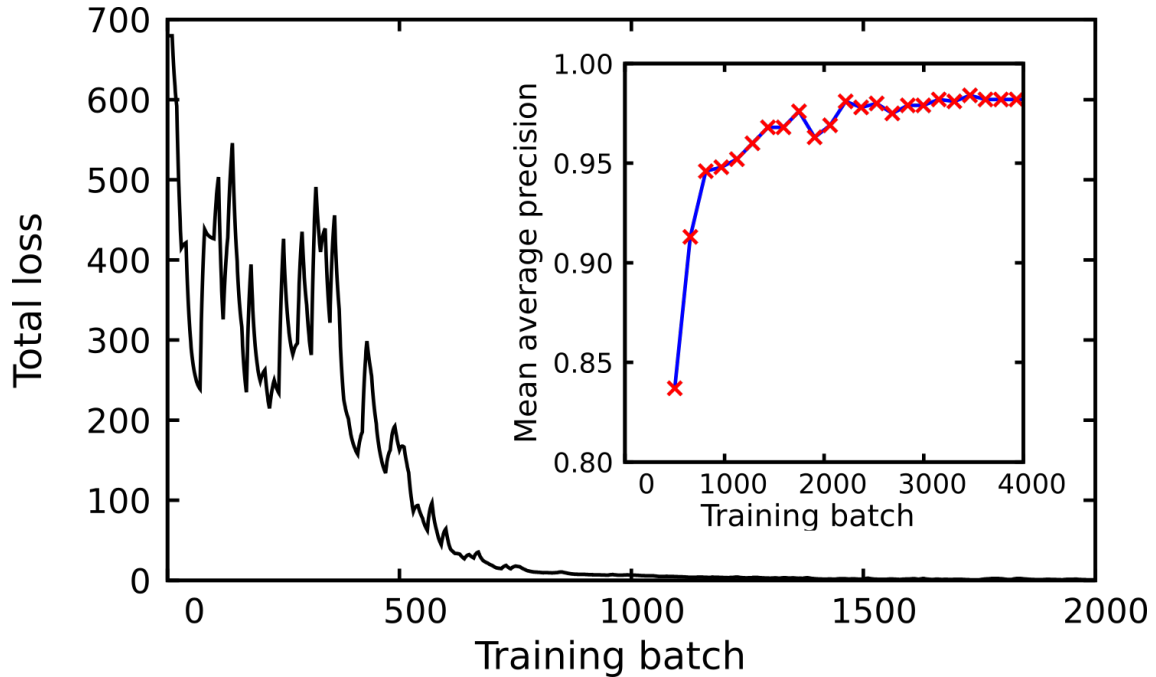


FIG. 4. Total loss function as the training progresses. In the inset we show mean average precision on the validation data computed during various stages of the training.

The accuracy of a trained network for object detection is measured by a metric called Average Precision (AP), a figure of merit between 0 and 1. The AP of a network can be computed using a separate validation data set and in our case, we reserved a fraction (5%) of the training data set as validation data set. In order to compute the AP, all the images of the validation data set are given as input to the network and all detected objects (droplets) are tabulated in descending order of their individual detection confidence score. Starting from the top of the table, for each detected object, precision and recall values are computed as follows.

$$P = \frac{TP}{TP + FP}, \quad R = \frac{TP}{TP + FN}. \quad (7)$$

Here, TP is the number of true positive detection (droplet does exist and it is detected), FP is the number of false positive detection (i.e. a droplet is detected but it doesn't exist ) and FN is the number of false negative detection (i.e., a droplet does exist but it is not detected).

To determine whether the detection is a true positive or a false positive, we use a quantity called *Intersection over Union (IoU)* value of the detection. In geometric terms, IoU is given by the area of intersection divided by area of union of ground truth bounding box, with predicted bounding box (see Fig. 5). We set the IoU threshold to 0.5, i.e. if the IoU is  $\geq 0.5$  the prediction is classified as a true positive.

After computing Precision and Recall for all the predictions in the validation data set, the Precision-Recall curve is plotted and the AP is computed as,  $AP = \int_0^1 p(r) dr$ . We also measured the mean average precision (mAP), defined as the average precision among all the classes of objects in the data set, as reported in the inset of Fig. 4. We observe that the mAP value monotonically increases as the training progresses and saturates to about 0.98 after a sufficient number of training batches, indicating that the training procedure achieves nearly perfect accuracy. At the end of the training, the optimised parameters of the network are saved and used for the Inference step, which we discuss next.

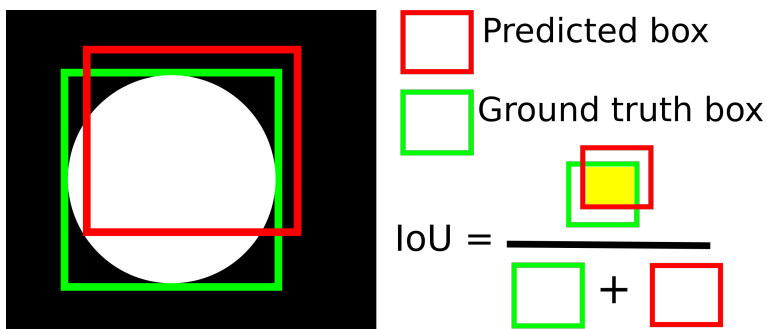


FIG. 5. Intersection over union of prediction (red box) and ground truth (green box).

### 3. Inference step

In the Inference step, the input data, i.e. the density maps produced by the LB simulations at each time step, are presented as an input to the trained network so that YOLO detects the droplets in the simulated image and passes this information along to the object

tracking algorithm (DeepSORT). Together, YOLO and DeepSORT detect and track the droplets at each time step, producing all the trajectories.

The particular network architecture can produce accurate trajectories even if the dimension in pixel of the input image is not exactly the same used during the training phase: training is a slow process that scales with the image size. It is a good advantage to reuse the coefficients of the Yolo network for images even 2x or 3x bigger, for which the training would have been significantly slower.

In the next section, we apply the network to two microfluidic cases simulated using the Lattice Boltzmann method described in Sec. II A, namely a straight and tapered channel, respectively. The first scenario should be easy for the detection (droplets are almost always circles) and tracking (droplets do not merge or split). The second case is a more interesting one, since the nozzle forces the droplets to aggregate and squeeze to fit the central channel: the shape of each droplet changes in time and some break-ups are present, which makes it a good test case.

### III. RESULTS AND DISCUSSION

To test our trained network we analysed video data generated for the two aforementioned applications. For the details, see the data access sheet. The first case (**Simple channel**) consists of a thin inlet channel in which droplets are continuously produced and flow downstream in the main microchannel (see Fig. 6). Sequences of images of size 850 X 250 pixels are generated and stacked to prepare a video file which serves as an input to the trained YOLO network for droplet detection.

The YOLO network analyses each frame of the video file, computing the bounding boxes for each detected droplet. The information of the bounding boxes, i.e. their size and location, is then passed to DeepSORT to track the droplets in the sequential images using a unique ID associated to each detected droplet. In Fig. 7 the inferred trajectories, as the centers of the bounding boxes, of the tracked droplets are shown. A video file (simple\_channel.mp4) showing the detection and tracking of the droplets is provided in the Supplementary Material.

The second system (**Tapered channel**) consists of a dense emulsion, flowing inside a tapered channel connected to a thin straight channel (see Fig. 8). Simulation output images of size 950 X 500 pixels were stacked to prepare input for the YOLO network. The predicted

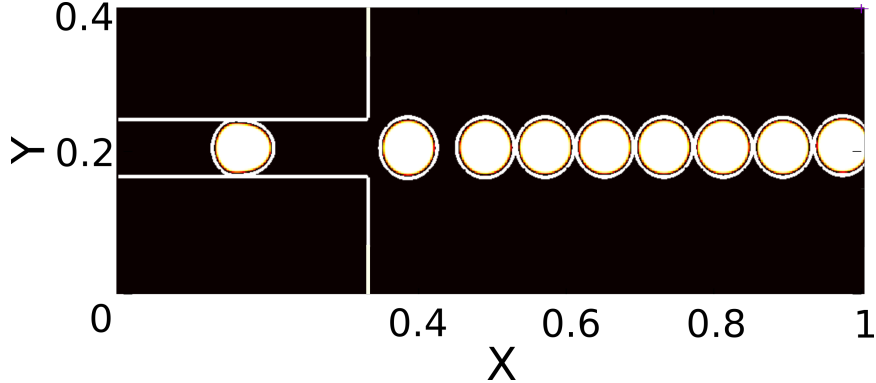


FIG. 6. Snapshot of the Simple channel. Droplets flow from left to right, in a almost straight horizontal path after leaving the channel at the left. The motion is quasi one-dimensional and leaves the droplets nearly circular.

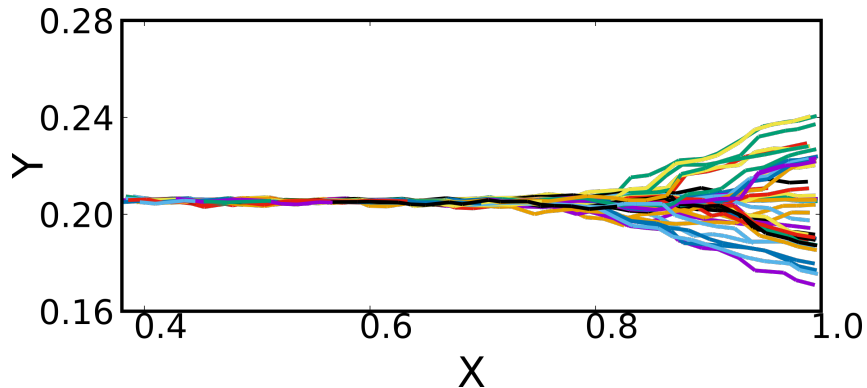


FIG. 7. Trajectories (centers of the bounding boxes) of the droplets for the Simple channel. Along the Y-axis small variations are correctly detected far enough from the channel. Each colour represents the trajectory of an individual droplet.

bounding boxes are shown in Fig. 9A and the trajectories of the droplets, i.e. the centers of the predicted bounding boxes, are compiled by analysing all the frames are shown in Fig. 9B. A video file (`tapered_channel.mp4`) of the detection and tracking process is also provided in the Supplementary Material.

### A. Computational performance

The computational time required to identify and track objects is an important factor for many applications. In Table I, we report the performances relative to the full track-and-

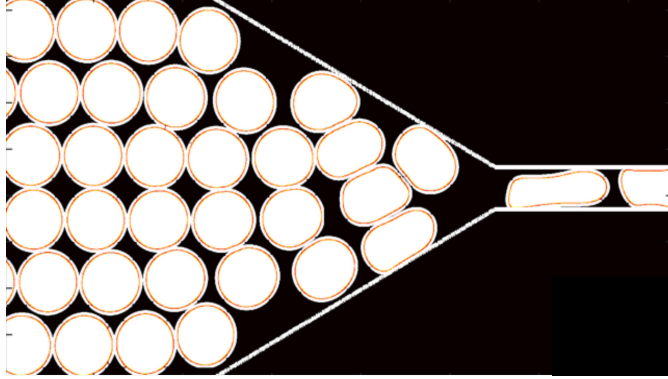


FIG. 8. A snapshot of the Tapered channel. Droplets enter the convergent nozzle from the left, pushing to enter the end of the channel at the right. The motion is now fully two-dimensional, with significant droplet deformations, thus setting a more demanding target to the Deep Learning procedure.

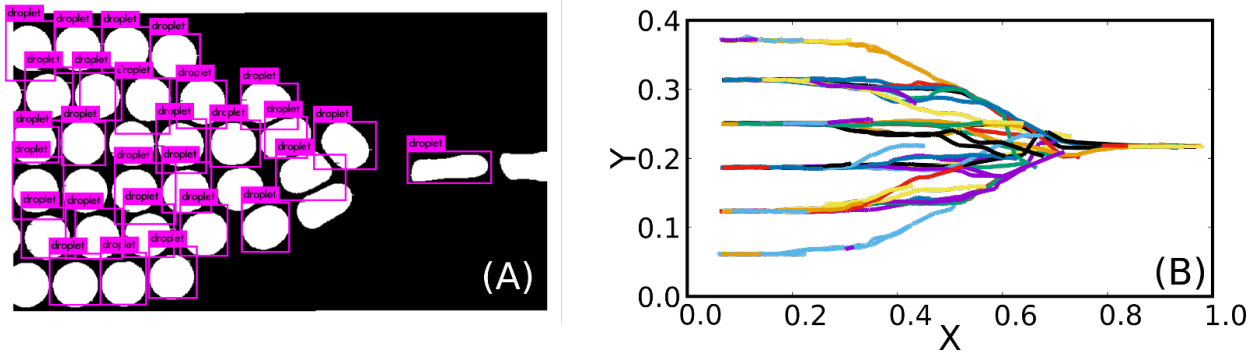


FIG. 9. (A) Droplet detected for the Tapered channel by YOLO network for the same snapshot shown in Fig. 8. (B) DeepSort uniquely labels each droplet to compute all the trajectories.

detect process on different computers, measuring the inference speed in frames per second (*fps*). We report the speed on two machines using only general purpose CPUs (in a typical configuration for a notebook and for a computing server), and using a middle level GPU for a desktop (NVIDIA RTX 2060 Super). From this table, it is clear that the inference proceeds at the significant speed of 400 frames per second on the machine powered by GPUs.

In another approach, feature extraction and clustering algorithms have been used to track moving objects at around 35fps [40] on multi-core CPUs. Even though it is not fair to compare the inference speed for algorithms with data sets of different complexity and using different computing machines, it is worthwhile to note that, with the method demonstrated

in this work, the complete process of identification and tracking of droplets can take place at much higher rates (few hundred *fps*) without trading-off the accuracy, and taking advantage of the existing machine learning frameworks highly optimized for the GPUs.

Machine	Inference speed	
	Simple channel	Tapered channel
CPU ( 1X Intel i3-2328M)	1.61 fps	0.69 fps
CPU (16X Intel Xeon Platinum 8176)	8.14 fps	5.10 fps
GPU (NVIDIA RTX 2060 Super)	400 fps	370 fps

TABLE I. Average inference speed for the two cases on various types of devices in frame per second (fps). Performances on GPU are almost 100x the values obtained with a full CPU implementation.

The application developed by training a cutting-edge deep learning model can be efficiently used to compute the trajectories of droplets in dense emulsion systems simulated by Lattice Boltzmann method or any other computational method capable of capturing the relevant physics. It is worth noting that in both cases explored, and especially in the case of the Tapered channel, the data used to train the network depart noticeably from those acquired via simulations. The fact that the network is nevertheless able to identify the droplets and efficiently track them over sequential frames bodes well for its generalisation to more complex applications, particularly for tracking deformable biological bodies in complex fluid flows. This will make the subject of future work.

#### IV. CONCLUSIONS

In this work, we demonstrated an automated procedure to adapt a cutting edge deep learning-based application, called YOLO and DeepSORT, to infer trajectories of droplets in dense emulsions in microchannels. We have shown that the deep network can effectively be trained with synthetic data, thereby bypassing the labour intensive process of acquiring the training data. The present tool performs competitively with state of the art object tracking and detection algorithms in terms of inference speed.

Extracting the information about the trajectories could also provide useful insights in the study of several other complex many-body systems, such as moving groups of animals

and biological microorganisms. We also plan to extend the ML procedure not only to detect droplets and track their trajectories, but also to exploit the latter data to infer the effective equations of motion of this complex many-body system, possibly using generative adversarial networks [41].

## V. ACKNOWLEDGEMENT

The research leading to these results has received funding from the European Research Council under the Horizon 2020 Programme Grant Agreement n. 739964 ("COPMAT"). A.M. acknowledges the CINECA Computational Grant ISCRA-C IsC83 - "SDROMOL", id. HP10CZXX6R under the ISCRA initiative, for the availability of high performance computing resources and support.

- 
- [1] Y. LeCun, Y. Bengio, and G. Hinton, *Nature* **521**, 436 (2015).
  - [2] T. M. Mitchell, *Machine Learning*, 1st ed., McGraw-Hill series in computer science (McGraw-Hill, 1997).
  - [3] P. V. Coveney, E. R. Dougherty, and R. R. Highfield, *Philosophical Transactions of the Royal Society A: Mathematical, Physical and Engineering Sciences* **374**, 20160153 (2016), <https://royalsocietypublishing.org/doi/pdf/10.1098/rsta.2016.0153>.
  - [4] S. Succi and P. V. Coveney, *Philosophical Transactions of the Royal Society A: Mathematical, Physical and Engineering Sciences* **377**, 20180145 (2019), <https://royalsocietypublishing.org/doi/pdf/10.1098/rsta.2018.0145>.
  - [5] J. Wu, Y. Yu, C. Huang, and K. Yu, *Proceedings of the IEEE Conference on Computer Vision and Pattern Recognition (CVPR)*, 3460 (2015).
  - [6] W. Rawat and Z. Wang, *Neural Computation* **29**, 2352 (2017).
  - [7] Darmatasia and M. I. Fanany, in *2017 5th International Conference on Information and Communication Technology (ICoICT7)* (2017) pp. 1–6.
  - [8] A. Hasan, S. Moin, A. Karim, and S. Shamshirband, *Math. Comput. Appl.* **23**, 11 (2018).
  - [9] A. M. Ramadhani and H. S. Goo, in *2017 7th International Annual Engineering Seminar (InAES)* (2017) pp. 1–4.

- [10] N. H. Tandel, H. B. Prajapati, and V. K. Dabhi, in *2020 6th International Conference on Advanced Computing and Communication Systems (ICACCS)* (2020) pp. 459–465.
- [11] G. Carleo, I. Cirac, K. Cranmer, L. Daudet, M. Schuld, N. Tishby, L. Vogt-Maranto, and L. Zdeborová, *Rev. Mod. Phys.* **91**, 045002 (2019).
- [12] A. W. Senior, R. Evans, J. Jumper, J. Kirkpatrick, L. Sifre, T. Green, C. Qin, A. Žídek, A. W. R. Nelson, A. Bridgland, H. Penedones, S. Petersen, K. Simonyan, S. Crossan, P. Kohli, D. T. Jones, D. Silver, K. Kavukcuoglu, and D. Hassabis, *Nature* **577**, 706 (2020).
- [13] I. Goodfellow, Y. Bengio, and A. Courville, *Deep Learning* (MIT Press, 2016) <http://www.deeplearningbook.org>.
- [14] C. L. Chen, A. Mahjoubfar, L.-C. Tai, I. K. Blaby, A. Huang, K. R. Niazi, and B. Jalali, *Scientific Reports* **6**, 21471 (2016).
- [15] Z. Guo, X. Li, H. Huang, N. Guo, and Q. Li, *IEEE Transactions on Radiation and Plasma Medical Sciences* **3**, 162 (2019).
- [16] H. Fujiyoshi, T. Hirakawa, and T. Yamashita, *IATSS Research* **43**, 244 (2019).
- [17] J. Xie, R. Liu, J. Luttrell, and C. Zhang, *Frontiers in Genetics* **10**, 80 (2019).
- [18] O. Sharir, Y. Levine, N. Wies, G. Carleo, and A. Shashua, *Phys. Rev. Lett.* **124**, 020503 (2020).
- [19] Y. Mahdi and K. Daoud, *Journal of Dispersion Science and Technology* **38**, 1501 (2017), <https://doi.org/10.1080/01932691.2016.1257391>.
- [20] J. W. Khor, N. Jean, E. S. Luxenberg, S. Ermon, and S. K. Y. Tang, *Soft Matter* **15**, 1361 (2019).
- [21] P. Hadikhani, N. Borhani, S. Hashemi, and D. Psaltis, *Scientific Reports* **9**, 8114 (2019).
- [22] M. Bernaschi, S. Melchionna, and S. Succi, *Rev. Mod. Phys.* **91**, 025004 (2019).
- [23] A. Montessori, M. Lauricella, N. Tirelli, and S. Succi, *Journal of Fluid Mechanics* **872**, 327 (2019).
- [24] A. Montessori, M. Lauricella, A. Tiribocchi, and S. Succi, *Physical Review Fluids* **4**, 072201 (2019).
- [25] A. Montessori, A. Tiribocchi, M. Lauricella, F. Bonaccorso, and S. Succi, *Phys. Rev. Fluids* **6**, 023606 (2021).
- [26] A. Montessori, A. Tiribocchi, M. Lauricella, F. Bonaccorso, and S. Succi, *Soft Matter* , (2021).



- [27] A. Montessori, A. Tiribocchi, F. Bonaccorso, M. Lauricella, and S. Succi, *Philosophical Transactions of the Royal Society A* **378**, 20190406 (2020).
- [28] S. Succi, *The Lattice Boltzmann Equation: For Complex States of Flowing Matter* (Oxford University Press, 2018).
- [29] T. Krüger, H. Kusumaatmaja, A. Kuzmin, O. Shardt, G. Silva, and E. M. Viggien, Springer International Publishing **10**, 978 (2017).
- [30] A. K. Gunstensen, D. H. Rothman, S. Zaleski, and G. Zanetti, *Physical Review A* **43**, 4320 (1991).
- [31] S. Leclaire, M. Reggio, and J.-Y. Trépanier, *Applied Mathematical Modelling* **36**, 2237 (2012).
- [32] M. Latva-Kokko and D. H. Rothman, *Physical Review E* **71**, 056702 (2005).
- [33] J. Redmon, S. Divvala, R. Girshick, and A. Farhadi, in *2016 IEEE Conference on Computer Vision and Pattern Recognition (CVPR)* (2016) pp. 779–788.
- [34] J. Redmon and A. Farhadi, ArXiv:1804.02767v1 (2018).
- [35] S. A. Sanchez, H. J. Romero, and A. D. Morales, *IOP Conference Series: Materials Science and Engineering* **844**, 012024 (2020).
- [36] N. Wojke, A. Bewley, and D. Paulus, in *2017 IEEE International Conference on Image Processing (ICIP)* (2017) pp. 3645–3649.
- [37] J. Redmon, “Darknet: Open source neural networks in c,” <http://pjreddie.com/darknet/>, year = 2013–2016.
- [38] <https://github.com/AlexeyAB/darknet>,.
- [39] Batches=10000, batch size=64, learning rate=0.001.
- [40] A. Keivani, J. Tapamo, and F. Ghayoor, in *2017 IEEE AFRICON* (2017) pp. 32–37.
- [41] L. Yang, C. Daskalakis, and G. E. Karniadakis, arXiv:2008.01915 (2020).